Revision 2

Interpretation of the infrared spectra of the lizardite-nepouite series in the near and middle infrared range

Fabien Baron and Sabine Petit

Université de Poitiers, CNRS-UMR 7285 IC2MP, HydrASA, Bât. 8, 5 rue Albert Turpain, TSA 51106, 86073 Poitiers Cedex 9, France

Abstract

A series of 1:1 silicate clays of the lizardite-nepouite series ($Si_2Mg_{3-x}Ni_xO_5(OH_4)$ with x = 0, 0.5, 1, 1.5, 2, 2.5, and 3) was synthesized at 220°C during 7 days from coprecipitated gels in hydrothermal conditions. A clear relationship was evidenced between the d(06-33) and the Ni/Mg ratio of the synthesized samples following a Vegard's law and suggested a rather random distribution of octahedral cations. For the first time, infrared spectra of this series were given in both near and mid infrared spectral regions (250 - 7500 cm^{-1}). Notably, the bands due to the OH stretching vibrations and those of their first overtones in the lizardite-nepouite series were attributed. The combination bands observed in the near infrared region for both end-members could be attributed thanks to combinations of two or three mid infrared features. Some of the observed combination bands are clearly linked to combination of different vibrational groups.

Infrared spectroscopy is simple to use and is a powerful tool to study the crystal-chemistry of garnierites. More broadly, the improvement of band attributions especially in near infrared contributes to develop the infrared analyses in field geology and remote sensing.

Keywords: lizardite, nepouite, infrared spectroscopy, near infrared, middle infrared, synthesis, nickel, clay minerals, serpentine, phyllosilicates, garnierite

Introduction

Nickel ore deposits are found in lateritic or sulphide forms. The major part of produced Ni comes from sulphide deposits (60 %) but Ni-laterite ores make up 60 to 70 % of the world's Ni resources (Butt and Cluzel 2013). Ni concentration in laterites results from an intensive weathering of ultramaphic rocks or their serpentinized equivalents under tropical or rainforest conditions like in New Caledonia (Wells et al. 2009) or Brazil (Mano et al. 2014). These deposits are divided in two ore types, an oxidized one and a hydrous silicate type currently named "Garnierite" (Faust 1966; Trescases 1975, 1979). The garnierite group is a general name for an intimate mixture of hydrous Ni-Mg silicates that commonly includes two or more of the following minerals: serpentine, talc, smectite and chlorite (Faust 1966; Brindley and Hang 1973; Springer 1974; Brindley et al. 1979; Gleeson et al. 2004). Ni-bearing minerals in the serpentine group are mainly lizardites and chrysotiles, whose Ni-analogs are nepouite and pecoraite. Nepouite was first described by Glassere (1907) as the Ni-lizardite analog, and Maksimovich (1973) showed the occurrence of the lizardite-nepouite series. The phyllosilicates belonging to the lizardite-nepouite series are generally mixed with other minerals in garnierite. The study of the crystal chemistry of these natural phyllosilicates is then uneasy. Moreover, as far as the authors are aware, spectral data concerning this series are not available in literature, notably in the near infrared (NIR) range (4000 - 7000 cm^{-1}) although NIR field spectrometers could widely be used by Ni-mining company for exploration. Field spectrometers are commonly used to distinguish mineral compositional variations which may vary with the composition of altering fluids, temperature and composition of host rocks in an alteration system. Mapping the mineralogical variations at both geological scale with field/airborne/spaceborn infrared spectrometer (Bowen et al. 2007; Di Tommaso and Rubinstein 2007; Chen et al. 2007; Brandmeier et al. 2013) using NIR data and at the microscopic scale with infrared

microspectroscopy (IRMS) (Robin et al. 2013) using MIR data, contributes to improve the understanding of the functioning of an alteration system and to determine the mineralization/alteration relationships. In order to map mineralogical variations in lateritic Ni ore deposit, spectral data in NIR range on the nepouite-lizardite series must be known. And generally, even if spectral data exist for clay minerals, any band interpretations in NIR range are made.

Therefore samples from the lizardite-nepouite series were synthesized to obtain pure reference samples for a Fourier transform infrared (FTIR) study, in both NIR and mid infrared (MIR) regions and band attributions were made.

Experimental

Clay synthesis

Samples of the lizardite-nepouite series were synthesized using a coprecipitated gel as starting material as in Baron et al. (2016). Coprecipitated gels of $Si_2Mg_{3-x}Ni_xO_7$ theoretical composition with x = 0, 0.5, 1, 1.5, 2, 2.5, and 3 were obtained by mixing solutions of sodium silicate, Mg and/or Ni chloride and sodium hydroxide (reaction 1).

(1) $2\ SiO_2Na_2O + (3\text{-}x)MgCl_2 + xNiCl_2 + 2\ NaOH \rightarrow Si_2\ Mg_{3-x}Ni_x\ O_7 + 6\ NaCl + H_2O$

After precipitation, the gel was collected by filtration and gently washed with deionized water to remove sodium chloride and then dried at 60°C for 48 hours before being crushed. 0.5 g of the powdered gel were placed into Teflon coated metallic bombs with 30 ml of deionized water and heated at 220°C during one week under equilibrium vapor pressure. The solid was separated from the solution by filtration and dried overnight at 60°C.

A synthetic Ni-Mg kerolite was also used in this study for comparison. The synthesis was done using the same way than for lizardite-nepouite series from a coprecipitated gel with $Si_4Mg_{1.5}Ni_{1.5}O_{11}$ theoretical composition obtained following the reaction (2):

(2) $4\ SiO_2Na_2O + 1.5MgCl_2 + 1.5NiCl_2 + 2\ HCl \rightarrow Si_4\ Mg_{1.5}Ni_{1.5}O_{11} + 8\ NaCl + H_2O$

Analysis

X-ray diffraction (XRD) powder patterns were performed with a Bruker D8 advance diffractometer (CuKα radiation, 40 kV and 40 mA) over the range 2 - 65°2θ, with 0.025°2θ step size and 0.6 seconds per step. The reflection (06-33) was recorded with a step of 0.025°2θ and a counting time of 4 seconds over the range 57 - 63°2θ. The position of the (06-33) reflection was determined by fitting XRD patterns with a pseudo-Voigt component in the Fityk software (Wojdyr 2010).

A Magna-IR 760 Nicolet spectrometer was used for mid infrared spectra over the range 400 - 4000 cm^{-1}, with an EverGlo source, a KBr beam splitter, a DTGS-KBr detector and a resolution of 4 cm^{-1} with co-additions of 100 scans. Over the range 200 - 500 cm^{-1}, a Thermo Scientific Nicolet 6700 FT-IR spectrometer was used with an EverGlo source, a CsI beam splitter, a DTGS-CsI detector and a resolution of 4 cm^{-1} with the co-additions of 100 scans. MIR spectra were obtained in transmission through KBr pellets, prepared with 1 mg of sample and 150 mg of KBr salt. The mixture was pressed during 5 minutes at 8 kbar and dried overnight in an oven at 110°C.

NIR spectra (3850 - 7500 cm^{-1}) were acquired with a Thermo Scientific Integrating Sphere (diffuse reflectance) equipped with an internal InGaAs detector, set on a Thermo Scientific Nicolet 6700 FT-IR spectrometer. A white light source was used, associated with a

CaF_2 beam splitter. The resolution was set at 4 cm^{-1} with the co-additions of 100 scans. Powder samples were analyzed directly on the integrating sphere without dilution.

The second derivative was carried out using the Savitzky–Golay filter (Savitzky and Golay 1964) in the Omnic™ software with a set of 13 points and a polynomial order of 3. The second derivative was used to determine the position of NIR and MIR bands, and was given in inverted form in this study to facilitate the reading of spectra.

The deviation in band position possibly induced by the second derivative method was estimated from a mathematical model. The model generated theoretical spectra by varying the relative intensities of 2 pseudo-Voigt components, with a 4 cm^{-1} resolution (as for experimental spectra). The second derivative of these theoretical spectra was carried out as described above for experimental spectra. The maximum deviation measured between the band positions introduced in the model and the band positions measured from the second derivative was +/- 3 cm^{-1}.

Results and discussion

XRD data

XRD powder patterns of all samples exhibited an intense (001) reflection at 7.39 Å and a (002) located at 3.67 Å for lizardite (x = 0) and at 3.64 Å for nepouite (x = 3), characterizing a 1:1 phyllosilicate structure. The (*hk*) reflections for lizardite (x = 0) and nepouite (x = 3) were situated at 4.51 and 4.50 Å (020), 2.59 and 2.63 Å (200), 2.47 Å (201), and at 1.537 and 1.529 Å (06-33), respectively (Fig. 1 and 2), revealing a trioctahedral structure. All (*hkl*) reflections were in agreement with data reported in literature for natural lizardite and nepouite samples (Whittaker and Zussman 1956; Mikheev 1957; Montoya and Baur 1963; Maksimovich 1973; Frondel and Ito 1975; Brindley and Brown 1980; Mellini 1982). XRD powder patterns revealed that no other crystalline phases were present for all samples.

The d(06-33) continuously shifted from 1.537 Å for lizardite (x = 0) to 1.529 Å for nepouite (x = 3) (Fig. 2). The d(06-33) value determined by fitting data with a single pseudo-Voigt component, was plotted versus the Ni contents (x), and a clear correlation was evidenced (Fig. 3) with the following regression line:

$$d(06\text{-}33)\ (Å) = -0.0026\ x + 1.5374 \quad (1)$$

This relation followed an apparent Vegard's law suggesting a random distribution of cations in the octahedral sheet of the synthesized samples. The progressive change of the d(06-33) along the lizardite-nepouite series is due to the atomic radii difference between Ni and Mg atoms in octahedral coordination (0.72 Å for Mg and 0.69 Å for Ni; Shannon 1976).

MIR data

The OH-stretching zone. The spectrum of the synthetic lizardite (x = 0) was similar to the natural one (Serna et al. 1979; Fuchs et al. 1998; Balan et al. 2002), with a complex band at 3698 cm^{-1} enlarged to 3688 cm^{-1} (which will be discussed later), and a broad band at 3648 cm^{-1} (Fig. 4). The former complex band at 3698 cm^{-1} corresponded to the in-phase stretching of the inner-surface Mg_3-OH groups and the latter at 3648 cm^{-1} to the two degenerate out-of-phase stretching modes of the inner-surface Mg_3-OH groups (Balan et al. 2002).

The increase of Ni contents in samples induced the progressive appearance of bands at 3686 cm^{-1}, 3668 cm^{-1}, and 3648 cm^{-1}. Finally, for nepouite (x = 3), only the band at 3648 cm^{-1} was present with a broad band at around 3610 cm^{-1} (Fig. 4). By analogy with the spectrum of the lizardite (x = 0) end-member, these two bands were assigned to the in-phase stretching of the inner-surface Ni_3-OH groups and to the two degenerate out-of-phase stretching modes of the inner-surface Ni_3-OH groups, respectively.

In trioctahedral phyllosilicates, each hydroxyl group is bonded to three octahedral cations and the nature of these cations modifies the stretching vibration of hydroxyl groups. In the lizardite-nepouite series, when Mg is partially replaced by Ni or conversely, four stretching OH (νOH) bands may be possibly distinguished due to the four possible cations combinations in the three neighboring octahedral sites as it is well known for talc series: νMg_3-OH, νMg_2R^{2+}-OH, $\nu MgR^{2+}{}_2$-OH and $\nu R^{2+}{}_3$-OH where R^{2+} is the substituted cation (Wilkins and Ito 1967; Petit et al. 2004; Petit 2005, 2006; Madejová et al. 2011). Consequently, the two bands at 3686 and 3668 cm^{-1} (Fig. 4) could be assigned to νMg_2Ni-OH and $\nu MgNi_2$-OH, respectively.

The 500-800 cm^{-1} region. The spectrum of lizardite (x = 0) revealed three bands at 634, 607 and 562 cm^{-1} (Fig. 4). These bands, characteristic of pure Mg-lizardite, were assigned, after IR spectra calculation, to longitudinal (LO) and transversal (TO) modes of in-plane bending of OH groups (Balan et al. 2002; Prencipe et al. 2009). Very often, natural lizardite samples contain some Fe^{2+} or Ni^{2+}, and exhibit a broad band rather than these three distinguishable bands (Balan et al. 2002). As a matter of fact, the three bands occurrence is a good criterion to easily determine the Mg-purity of lizardite. For nepouite (x = 3), a broad and dissymmetric band at 674 cm^{-1} with a shoulder at 600 cm^{-1} was observed. The intermediary samples ($0.5 < x < 2.5$) of the solid-solution exhibited a broad and complex multicomponent band (Fig. 4).

The lattice bands. Two main bands located at 984 and near 1080 cm^{-1} (Fig. 4) were observed for all samples (Fig. 4). These bands were attributed to the two degenerate equatorial stretching of Si-O bonds and the symmetric stretch of apical Si-O bonds, respectively (Balan et al. 2002). The former band remained at 984 cm^{-1} whatever the Ni content (x), whereas the latter band was at 1084 cm^{-1} for lizardite (x = 0) and moves progressively to 1075 cm^{-1} for nepouite (x = 3). A small shoulder at 1024 cm^{-1} was observed for Mg-rich samples and disappeared with the increase of Ni content (x) (Fig. 4). This shoulder was attributed to a LO mode (Prencipe et al.

2009) and could not be attributed to small amount of chrysotile because it would be associated to an intense band at 960 cm^{-1} (Farmer 1974; Anbalagan et al. 2010; Madejová et al. 2011).

The lizardite (x = 0) spectrum exhibited bands at 454, 436, 400, 383, and 303 cm^{-1} while the nepouite (x = 3) spectrum exhibited bands at 455, 426, 377, 361, and 318 cm^{-1} (Fig. 4). The lizardite (x = 0) experimental spectrum was in agreement with the calculated spectra (Balan et al. 2002; Prencipe et al. 2009). For the intermediary samples ($0.5 < x < 2.5$), the bands moved progressively and were at intermediate position between those of the lizardite (x = 0) and nepouite (x = 3) end-members.

NIR data

The occurrence of a broad and intensive OH-water combination band around 5205 cm^{-1} (Hunt and Salisbury 1970) in all spectra (Supplementary file a), revealed the relatively high water content in samples, as it is very common for synthetic phyllosilicates. The high hydration state of synthetic phyllosilicates is generally due to their small particle size (Dumas et al. 2013).

The first OH overtone region. By analogy with the MIR νOH region, the bands at 7226, 7198, 7164 and 7124 cm^{-1} (Fig. 5) were assigned to $2\nu Mg_3$-OH, $2\nu Mg_2Ni$-OH, $2\nu MgNi_2$-OH and $2\nu Ni_3$-OH. As for the MIR region, the presence of four 2νOH bands with relative intensities varying continuously all along the solid-solution series argued for a rather random distribution of Ni and Mg atoms in the octahedral sheet of the samples. The lack of a band at 7236 cm^{-1} confirmed the absence of chrysotile (Madejová et al. 2011).

The anharmonicity constant between the νOH and 2νOH wavenumbers of the lizardite-nepouite series is X = -85.6 cm^{-1}, that is the same value measured by Petit et al. (2004) for talcs and others phyllosilicates (Fig. 6). This relation gives confidence for the above NIR assignments.

The NIR spectrum of lizardite (x = 0), exhibited a shoulder at 7203 cm^{-1} which could not be attributed to the $2\nu Mg_2NiOH$ overtone (Fig. 5). This band may be attributed to the overtone of the shoulder at 3688 cm^{-1} observed in the MIR spectrum according to the anharmonicity constant value of -86.5 cm^{-1}. These bands may be due to vibrations of structural Mg_3-OH groups in lizardite (x = 0). In theory, only the transverse mode (TO) is IR active for infinite crystals. However when crystals exhibit one (or more) dimension much smaller than the wavelength of the IR radiations (0.78 - 1000 μm), both the LO and TO modes are observed (Farmer 1998; Balan et al. 2002; Prencipe et al. 2009). Therefore the wavenumber of the observed IR bands are strongly dependent on the lizardite particles size. Similar lizardites were synthesized and exhibited essentially small rounded particles with 40 nm in diameter and few lathed particles with 0.2 μm in length (Mondésir and Decarreau 1987). So, for lizardite (x = 0), the bands at 3698 and 7226 cm^{-1} and the shoulders at 3688 and 7203 cm^{-1} possibly correspond to the LO-TO splitting of the Mg_3OH groups (Farmer 1998; Prencipe et al. 2009).

The OH combination bands. In the 3850 - 4500 cm^{-1} region, the lizardite (x = 0) spectrum exhibited two main bands located at 4305 and 4275 cm^{-1} while for nepouite (x = 3), only one main asymmetric broad band was observed at 4280 cm^{-1} (Fig. 5). In the 4500 and 5000 cm^{-1} region (Fig. 5) two bands at 4780 and 4709 cm^{-1} were observed in the lizardite (x = 0) spectrum, which shifted with increasing Ni contents to 4722 and 4650 cm^{-1}, respectively.

Origins of combination bands for lizardite (x = 0) and nepouite (x = 3) end members. The combination bands due to water (5000 – 5500 cm^{-1}) are well known for clay minerals (Cariati et al. 1981, 1983a; b). But the observed combination bands in the 3850 – 5000 cm^{-1} range are generally not assigned, except for the combination bands arising from combination of stretching and bending structural OH groups for some clay minerals (Frost et al. 2002; Gates 2008; Bishop et al. 2008; Andrieux and Petit 2010; Madejová et al. 2011; Petit et al. 2015).

The wavenumber of observed combination bands was measured for both lizardite (x = 0) and nepouite (x = 3) end-members using the second derivative treatment of spectra (Fig. 7.a for lizardite (x = 0) and Fig. 7.b for nepouite (x = 3)). Generally in infrared spectroscopy, the signal treatment like the second derivative is more suitable to reveal the band position than the decomposition process, due to the relatively broad and complex bands (Gionis et al. 2006; Chryssikos et al. 2009). The 21 observed features (Fig. 7) were listed in Table 1 for lizardite (x = 0) and in Table 2 for nepouite (x = 3).

Absorption bands in the combination region result from the sharing of IR radiation energy between two or more fundamental vibrations which are observed in MIR range (Ciurczak 2006). Consequently, a second derivative treatment was realized on MIR spectra of each end-members in order to reveal the position of MIR features (Fig. 8.a for lizardite (x = 0) and Fig. 8.b for nepouite (x = 3)). First, all combinations between one νOH and one lattice or δOH bands were calculated (Table 3.a for lizardite (x = 0) and Table 3.b for nepouite (x = 3)). The wavenumber of the combination band corresponds then more or less to the summation of the wavenumber of the implicated vibrations. The proposed attribution of bands was made using a difference limit (Δ) arbitrary fixed at 10 cm^{-1} between calculated and observed NIR band positions (Table 1 and 2). This relatively high limit value is assumed to be due to the shift which could result from the actual position of a band and the position of the band determined by the second derivative of NIR and MIR spectra. The difference limit is also assumed to include a possible contribution of anharmonicity.

Most of the bands observed in the NIR spectra of lizardite (x = 0) (Table 1) and nepouite (x = 3) (Table 2) can be explained by the summation of two MIR bands (bands # 1, 3 to 12, 14, and 19 to 21 for lizardite (x = 0) and bands # 1 to 9, 11 to 13, and 19 to 21 for nepouite (x = 3)). Some of them could have several origins (bands # 6, 7, 9, and 19 for lizardite (x = 0) and bands #

235 2, 4 to 7, and 11 for nepouite (x = 3)). For nepouite (x = 3), the proximity between NIR bands (14
236 cm^{-1} between bands # 8 and 9; and 15 cm^{-1} between bands # 5 and 6), did not allow to
237 discriminate between the two possible combinations (e.g. bands # 8 and 9 and bands # 5 and 6,
238 respectively - Table 2).

239 A rather good agreement is observed between the experimental NIR spectra and the
240 calculated NIR band positions for both lizardite (x = 0) and nepouite (x = 3). But some of the
241 observed NIR bands remained unexplained (# 2, 13, 15 to 18 for lizardite (x = 0) and # 10, 14 to
242 18 for nepouite (x = 3)). The band # 2 in lizardite (x = 0) spectrum cannot be explained by any
243 combination within the fixed difference limit (Δ). However, this band is at an intermediate
244 position between NIR bands # 1 and 3 and then could result from an overlap of these two bands.
245 Such an overlap may generate a broad band centered at the position of the observed band # 2.

246 Note that some of the calculated combinations (Table 3) were not observed on the NIR
247 spectra of both end-members. These combinations may be forbidden and are not valid or maybe
248 of too low intensity and hidden by another band.

249 When it was possible to identify the MIR features corresponding to a same vibrational
250 group in both lizardite (x = 0) and nepouite (x = 3) end-members spectra, they were labelled with
251 the same letter (a to i - Fig. 8). The attribution of NIR combinations was then compared between
252 both end-members (Table 4). The combination bands concerning equivalent vibrational groups
253 for lizardite (x = 0) and nepouite (x = 3) spectra give confidence on the attribution of the
254 observed NIR combination bands.

255 In both end-member spectra, some bands between 4300 and 4600 cm^{-1} could not be
256 explained by combinations between two MIR features. Combinations with three MIR features
257 were tested (Supplementary files b and c for lizardite (x = 0) and nepouite (x = 3), respectively)
258 to tentatively attribute the observed NIR bands in the 4300 - 4600 cm^{-1} range. Many

combinations between three MIR features could explain the observed NIR bands which were not attributed previously. These combinations between three MIR features could correspond to combinations between one MIR feature and one NIR feature (previously attributed; Table 1 and 2) localized in the low wavenumbers range of NIR spectra (3850 - 4300 cm^{-1}).

To simplify the attribution of observed NIR bands for both end-members and to reduce the error of position, combinations between one MIR feature with one observed NIR feature in the low wavenumbers range of the NIR spectra were made (Table 5 for lizardite (x = 0) and Table 6 for nepouite (x = 3)). The bands # 13, 15, 16, 17, and 18, in the lizardite (x = 0) spectrum and bands # 14, 15, 16, 17, and 18, in the nepouite (x = 3) spectrum, could be explained by several combinations with one MIR and one NIR features. Note that the bands observed in the 4300 - 4600 cm^{-1} range could not be explained by combinations of two MIR features (Table 1 and 2 for lizardite (x = 0) and nepouite (x = 3), respectively) but they could be explained by combinations with three MIR features. More precisely, all these bands could be explained by combinations between observed NIR features in the low wavenumbers range of the NIR spectra and the MIR band noted c (at 401 cm^{-1} for lizardite (x = 0) and at 379 cm^{-1} for nepouite (x = 3), Fig. 8). The origin of this MIR band noted c, was not found in the literature as far as the authors are aware. The complex pattern of IR spectra in the 400 - 200 cm^{-1} was assumed to involve mixed vibrations involving the silicon-oxygen network, the octahedral cations and the hydroxyl group (Farmer 1974).

Implications

NIR spectroscopy is widely used for remote-sensing and field studies to identify clay minerals. However, NIR spectra are often complex and uninterpreted even for monomineral samples, especially in the combination region where the origin of bands is unknown for many

clay minerals. Substantial progress in the interpretation of the IR spectra can be realized from chemical series of monomineral samples with controlled distribution of atoms. Hydrothermal syntheses allowed to obtain those chemical series. In this paper, samples from the lizardite-nepouite series with a random distribution of Ni and Mg were synthesized to obtain robust reference spectra. Because the $2\nu R^{2+}{}_3$-OH vibrations were attributed, these reference spectra could be used in field geology to discriminate the Ni distribution in single phase or in intimate mixture between 1:1 (lizardite-nepouite) and 2:1 (kerolite-pimelite) phyllosilicates from lateritic nickel ore deposits as in garnierite. Note that the 2νOH in NIR region provided more resolved features compared to the νOH in MIR region and may help to distinguish between the 1:1 and the 2:1 Mg-Ni phyllosilicates even if partial overlapping of bands (Fig. 9).

The bands observed in the combination region were attributed with confidence by comparing both lizardite (x = 0) and nepouite (x = 3) spectra. The observed combination bands result from combinations of two or three MIR features. Those combined MIR features can result from the same vibrational group (e.g. combination between δOH and νOH vibrations) or from different vibrational groups (e.g. combination between νOH and νSi-O vibrations). The work of interpretation by analogy using chemical series is essential for aiding the interpretation of IR spectra. Indeed calculations of theoretical spectra (e.g. Balan et al. 2002; Prencipe et al. 2009) cannot be performed up to now for minerals which contain transition metals (e.g. Ni, Fe…).

Acknowledgments

We gratefully acknowledge A. Decarreau for his helpful discussions on a preliminary version. We are grateful to J. Yvon and an anonymous reviewer for their constructive contributions.

References

Anbalagan, G., Sivakumar, G., Prabakaran, A.R., and Gunasekaran, S. (2010) Spectroscopic characterization of natural chrysotile. Vibrational Spectroscopy, 52, 122–127.

Andrieux, P., and Petit, S. (2010) Hydrothermal synthesis of dioctahedral smectites: The Al–Fe^{3+} chemical series. Part I: Influence of experimental conditions. Applied Clay Science, 48, 5–17.

Balan, E., Saitta, A.M., Mauri, F., Lemaire, C., and Guyot, F. (2002) First-principles calculation of the infrared spectrum of lizardite. American Mineralogist, 87, 1286–1290.

Baron, F., Pushparaj, S.S.C., Fontaine, C., Sivaiah, M.V., Decarreau, A., and Petit, S. (2016) Microwave-assisted hydrothermal synthesis of Ni-Mg layered silicate clays. Current Microwave Chemistry, 3, (In press).

Bishop, J.L., Lane, M.D., Dyar, M.D., and Brown, A.J. (2008) Reflectance and emission spectroscopy study of four groups of phyllosilicates: smectites, kaolinite-serpentines, chlorites and micas. Clay Minerals, 43, 35–54.

Bowen, B.B., Martini, B.A., Chan, M.A., and Parry, W.T. (2007) Reflectance spectroscopic mapping of diagenetic heterogeneities and fluid-flow pathways in the Jurassic Navajo Sandstone. AAPG Bulletin, 91, 173–190.

Brandmeier, M., Erasmi, S., Hansen, C., Höweling, A., Nitzsche, K., Ohlendorf, T., Mamani, M., and Wörner, G. (2013) Mapping patterns of mineral alteration in volcanic terrains using ASTER data and field spectrometry in Southern Peru. Journal of South American Earth Sciences, 48, 296–314.

328 Brindley, G.W., Bish, D.L., and Wan, H.M. (1979) Compositions, structures, and properties of
329 nickel-containing minerals in the kerolite-pimelite series. American Mineralogist, 64,
330 615–625.

331 Brindley, G.W., and Brown, G. (1980) Crystal structures of clay minerals and their X-ray
332 identification, 495 p. The Mineralogical Society, London.

333 Brindley, G.W., and Hang, P.T. (1973) The nature of garnierites: I, structures, chemical
334 compositions and color characteristics. Clays and Clay Minerals, 21, 27–40.

335 Butt, C.R.M., and Cluzel, D. (2013) Nickel laterite ore deposits: Weathered serpentinites.
336 Elements, 9, 123–128.

337 Cariati, F., Erre, L., Micera, G., Piu, P., and Gessa, C. (1983a) Effects of layer charge on the
338 near-infrared spectra of water molecules in smectites and vermiculites. Clays and Clay
339 Minerals, 31, 447–449.

340 Cariati, F., Erre, L., Micera, G., Piu, P., and Gessa, C. (1983b) Polarization of water molecules in
341 phyllosilicates in relation to exchange cations as studied by near infrared spectroscopy.
342 Clays and Clay Minerals, 31, 155–157.

343 Cariati, F., Erre, L., Micera, G., Piu, P., and Gessa, C. (1981) Water molecules and hydroxyl
344 groups in montmorillonites as studied by near infrared spectroscopy. Clays and Clay
345 Minerals, 29, 157–159.

346 Chen, X., Warner, T.A., and Campagna, D.J. (2007) Integrating visible, near-infrared and short-
347 wave infrared hyperspectral and multispectral thermal imagery for geological mapping at
348 Cuprite, Nevada. Remote Sensing of Environment, 110, 344–356.

Chryssikos, G.D., Gionis, V., Kacandes, G.H., Stathopoulou, E.T., Suárez, M., García-Romero, E., and Río, M.S.D. (2009) Octahedral cation distribution in palygorskite. American Mineralogist, 94, 200–203.

Ciurczak, E.W. (2006) Near-infrared spectroscopy, In S. Ahuja and N. Jespersen Eds., Modern instrumental analysis, p. 157–176. Elsevier, Amsterdam.

Dumas, A., Martin, F., Le Roux, C., Micoud, P., Petit, S., Ferrage, E., Brendlé, J., Grauby, O., and Greenhill-Hooper, M. (2013) Phyllosilicates synthesis: a way of accessing edges contributions in NMR and FTIR spectroscopies. Example of synthetic talc. Physics and Chemistry of Minerals, 40, 361–373.

Farmer, V.C. (1998) Differing effects of particle size and shape in the infrared and Raman spectra of kaolinite. Clay Minerals, 33, 601–604.

Farmer, V.C. (1974) The infrared spectra of minerals, 539 p. The Mineralogical Society, London.

Faust, G.T. (1966) The hydrous nickel-magnesium silicates - The garnierite group. American Mineralogist, 51, 279–298.

Frondel, C., and Ito, J. (1975) Zinc-rich chlorites from Franklin, New Jersey. Neues Jahrbuch für Mineralogie. Abhandlungen, 123, 111–115.

Frost, R.L., Kloprogge, J.T., and Ding, Z. (2002) Near-infrared spectroscopic study of nontronites and ferruginous smectite. Spectrochimica Acta Part A: Molecular and Biomolecular Spectroscopy, 58, 1657–1668.

Fuchs, Y., Linares, J., and Mellini, M. (1998) Mössbauer and infrared spectrometry of lizardite-1T from Monte Fico, Elba. Physics and Chemistry of Minerals, 26, 111–115.

Gates, W.P. (2008) Cation mass-valence sum (CM-VS)approach to assigning OH-bending bands in dioctahedral smectites. Clays and Clay Minerals, 56, 10–22.

Gionis, V., Kacandes, G.H., Kastritis, I.D., and Chryssikos, G.D. (2006) On the structure of palygorskite by mid- and near-infrared spectroscopy. American Mineralogist, 91, 1125–1133.

Glassere, E. (1907) Note sur une espèce minérale nouvelle, la Népouite, silicate hydraté de nickel et de magnésie. Bulletin de la Société Française de Minéralogie, 30, 17–28.

Gleeson, S.A., Herrington, R.J., Durano, J., Velasquez, C.A., and Koll, G. (2004) The mineralogy and geochemistry of the Cerro Matoso S.A. Ni-laterite deposit, Montelibano, Colombia. Economic Geology, 99, 1197–1213.

Hunt, G.R., and Salisbury, J.W. (1970) Visible and infrared spectra of minerals and rocks: I. Silicate minerals. Modern Geology, 1, 283–300.

Madejová, J., Balan, E., and Petit, S. (2011) Advances in the characterization of industrial minerals, In Christidis, G.E. Ed., Application of vibrational spectroscopy to the characterization of phyllosilicates and other industrial minerals, p. 171–226. The Mineralogical Society, London.

Maksimovich, Z. (1973) Izomorfnaya seriya lizardit-nepuit (The isomorphous series lizardite-nepouite). Zapiski Vsesoyuznogo Mineralogicheskogo Obshchestva, 102, 143–149.

Mano, E.S., Caner, L., Petit, S., Chaves, A.P., and Mexias, A.S. (2014) Mineralogical characterization of Ni-bearing smectites from Niquelândia, GO - Brazil. Clay Minerals, 62, 325–336.

Mellini, M. (1982) The crystal structure of lizardite 1T; hydrogen bonds and polytypism. American Mineralogist, 67, 587–598.

Mikheev, V.I. (1957) X-Ray determination of minerals (Rentgenovskii Opredelitel' Mineralov), 820 p. Gosgeoltekhizdat, Moscow.

Mondésir, H., and Decarreau, A. (1987) Synthèse entre 25 et 200°C de lizardites Ni-Mg. Mesure des coefficients de partage solide-solution aqueuse pour le couple Ni-Mg dans les lizardites. Bulletin de Minéralogie, 110, 409–426.

Montoya, J.W., and Baur, G.S. (1963) Nickeliferous serpentines, chlorites, and related minerals found in two lateritic ores. American Mineralogist, 48, 1227–1238.

Petit, S. (2006) Fourier transform infrared spectroscopy, In Bergaya, F. and Lagaly, G. Eds., Handbook of clay science, p. 909–918. Elsevier, Amsterdam.

Petit, S. (2005) The application of vibrational spectrocopy to clay minerals and layered double hydroxides, In Theo Kloprogge, J. Ed., Crystal-chemistry of Talc: A NIR and MIR spectroscopic appraoch, p. 41–64. The Clay Minerals Society, Aurora, CO.

Petit, S., Decarreau, A., Gates, W., Andrieux, P., and Grauby, O. (2015) Hydrothermal synthesis of dioctahedral smectites: The Al–Fe^{3+} chemical series. Part II: Crystal-chemistry. Applied Clay Science, 104, 96–105.

Petit, S., Decarreau, A., Martin, F., and Buchet, R. (2004) Refined relationship between the position of the fundamental OH stretching and the first overtones for clays. Physics and Chemistry of Minerals, 31, 585–592.

Prencipe, M., Noel, Y., Bruno, M., and Dovesi, R. (2009) The vibrational spectrum of lizardite-1T [$Mg_3Si_2O_5(OH)_4$] at the Γ point: A contribution from an ab initio periodic B3LYP calculation. American Mineralogist, 94, 986–994.

Robin, V., Petit, S., Beaufort, D., and Prêt, D. (2013) Mapping kaolinite and dickite in sandstone thin sections using infrared microspectroscopy. Clays and Clay Minerals, 61, 141–151.

Savitzky, A., and Golay, M.J.E. (1964) Smoothing and differentiation of data by simplified least squares procedures. Analytical Chemistry, 36, 1627–1639.

Serna, C.J., White, J.L., and Velde, B.D. (1979) The effect of aluminium on the infra-red spectra of 7 Å trioctahedral minerals. Mineralogical Magazine, 43, 141–147.

Shannon, R. (1976) Revised effective ionic radii and systematic studies of interatomic distances in halides and chalcogenides. Acta Crystallographica Section A, 32, 751–767.

Springer, G. (1974) Compositional and structural variations in garnierites. Canadian Mineralogist, 12, 381–388.

Di Tommaso, I., and Rubinstein, N. (2007) Hydrothermal alteration mapping using ASTER data in the Infiernillo porphyry deposit, Argentina. Ore Geology Reviews, 32, 275–290.

Trescases, J.J. (1975) L'Évolution géochimique supergène des roches ultrabasiques en zone tropicale formation des gisements nickélifères de Nouvelle-Calédonie, 259 p. Office de la recherche scientifique et technique outre-mer, Paris.

Trescases, J.J. (1979) Remplacement progressif des silicates par les hydroxydes de fer et de nickel dans les profils d'altération tropicale des roches ultrabasiques; accumulation résiduelle et épigénie. Sciences Géologique, Bulletin, 32, 181–188.

Wells, M.A., Ramanaidou, E.R., Verrall, M., and Tessarolo, C. (2009) Mineralogy and crystal chemistry of "garnierites" in the Goro lateritic nickel deposit, New Caledonia. European Journal of Mineralogy, 21, 467–483.

Whittaker, E.J.W., and Zussman, J. (1956) The characterization of serpentine minerals by X-ray diffraction. Mineralogical Magazine, 31, 107–126.

Wilkins, R.W.T., and Ito, J. (1967) Infrared spectra of some synthetic talcs. American Mineralogist, 52, 1649–1661.

Wojdyr, M. (2010) Fityk: a general-purpose peak fitting program. Journal of Applied Crystallography, 43, 1126–1128.

447 **Figure captions:**

448

449 **Figure 1.** Powder XRD patterns of synthesized lizardite-nepouite series ($Si_2Mg_{3-x}Ni_xO_5(OH)_4$).

450

451 **Figure 2.** XRD patterns of (06-33) reflections of synthesized lizardite-nepouite series (Si_2Mg_{3-}
452 $_xNi_xO_5(OH)_4$).

453

454 **Figure 3.** d(06-33) values (Å) versus Ni content (x) in lizardite-nepouite synthetic series (Si_2Mg_{3-}
455 $_xNi_xO_5(OH)_4$). The size of symbol denotes the error on the d(06-33) measurements.

456

457 **Figure 4.** Selected regions of the MIR spectra of synthesized lizardite-nepouite series (Si_2Mg_{3-}
458 $_xNi_xO_5(OH)_4$).

459

460 **Figure 5.** Selected regions of the NIR spectra of synthesized lizardite-nepouite series (Si_2Mg_{3-}
461 $_xNi_xO_5(OH)_4$).

462

463 **Figure 6.** Wavenumbers of the ν OH bands versus wavenumbers of the 2ν OH first overtones for
464 the synthesized lizardite-nepouite samples - this study (●), for various OH groups in talc (□ and
465 Ni-Mg ■) (Petit et al. 2004) and for palygorskite (Δ) (Gionis et al. 2006). The size of symbols
466 denotes the error on the wavenumber measurements.

467

468 **Figure 7.** NIR spectra in the combination region and their second derivative of lizardite (x = 0)
469 ($Si_2Mg_3O_5(OH)_4$) (a), and nepouite (x = 3) ($Si_2Ni_3O_5(OH)_4$) (b). Numbers 1 to 21 correspond to

combination bands listed in table 1 for lizardite (x = 0) and in table 2 for nepouite (x = 3). In grey, combination band positions from the second derivative NIR spectra.

Figure 8. Second derivative of MIR spectra of lizardite (x = 0) ($Si_2Mg_3O_5(OH)_4$) (a), and nepouite (x = 3) ($Si_2Ni_3O_5(OH)_4$) (b). Letters correspond to the same vibrational group for each end-member.

Figure 9. First OH-overtones (2νOH) region of synthesized Ni-lizardite ($Si_2Mg_{1.5}Ni_{1.5}O_5(OH)_4$) and Ni-kerolite ($Si_4Mg_{1.5}Ni_{1.5}O_{10}(OH)_2.nH_20$).

494 **Tables:**

495

496 Table 1. Observed NIR combination band positions of lizardite (x = 0) and calculated NIR
497 combination band positions from combination with two MIR features. Δ corresponds to the
498 difference between the calculated and the observed combination band positions. † corresponds to
499 small identified features (see Fig. 7a).

Band #	Observed NIR bands (cm^{-1})	Combination with two MIR features (cm^{-1})				Calculated NIR bands (cm^{-1})	Δ (cm^{-1})
1	3958	302	+	3648	=	3950	8
2	3985						
3	4001	302	+	3695	=	3997	4
4	4032	380	+	3648	=	4028	4
5†	4049†	401	+	3648	=	4049	0
6	4077	380	+	3695	=	4075	2
		434	+	3648	=	4082	5
7	4121	434	+	3695	=	4129	8
		481	+	3648	=	4129	8
8	4163	458	+	3695	=	4153	10
9	4199	504	+	3695	=	4199	0
		554	+	3648	=	4202	3
10†	4240†	554	+	3695	=	4249	9
11	4274	635	+	3648	=	4283	9
12	4307	607	+	3695	=	4302	5
13	4363						
14†	4396†	693	+	3695	=	4388	8
15	4409						
16	4442						
17†	4487†						
18†	4531†						
19	4675	974	+	3695	=	4669	6
		1024	+	3648	=	4672	3
20	4709	1024	+	3695	=	4719	10
21	4781	1086	+	3695	=	4781	0

500

501

Table 2. Observed NIR combination band positions of nepouite (x = 3) and calculated NIR combination band positions from combination with two MIR features. Δ corresponds to the difference between the calculated and the observed combination band positions. † corresponds to small identified features (see Fig. 7b).

Band #	Observed NIR bands (cm^{-1})	Combination with two MIR features (cm^{-1})				Calculated NIR bands (cm^{-1})	Δ (cm^{-1})
1	3934	318	+	3608	=	3926	8
2	3971	318	+	3649	=	3967	4
		357	+	3608	=	3965	6
3	4000	357	+	3649	=	4006	6
4†	4037†	379	+	3649	=	4028	9
		427	+	3608	=	4035	2
5	4056	404	+	3649	=	4053	3
		456	+	3608	=	4064	8
6†	4071†	427	+	3649	=	4076	5
		456	+	3608	=	4064	7
7	4097	456	+	3649	=	4105	8
		493	+	3608	=	4101	4
8	4136	493	+	3649	=	4142	6
9	4150	493	+	3649	=	4142	8
10†	4182†						
11	4277	628	+	3649	=	4277	0
		676	+	3608	=	4284	7
12	4297	652	+	3649	=	4301	4
13	4321	676	+	3649	=	4325	4
14	4348						
15	4383						
16†	4426†						
17	4447						
18†	4522†						
19	4652	1049	+	3608	=	4657	5
20	4698	1049	+	3649	=	4698	0
21	4722	1079	+	3649	=	4728	6

509 Table 3. Calculated combinations (in cm^{-1}) between νOH and lattice or δOH bands; a: for
510 lizardite (x = 0) and b: for nepouite (x = 3).

a	lizardite (x = 0)		**b**	nepouite (x = 3)	
Lattice or δOH bands	νOH bands		Lattice or δOH bands	νOH bands	
	3648	3695		3608	3649
1086	4734	4781	1079	4687	4728
1024	4672	4719	1049	4657	4698
974	4622	4669	1015	4623	4664
693	4341	4388	978	4586	4627
635	4283	4330	676	4284	4325
607	4255	4302	652	4260	4301
554	4202	4249	628	4236	4277
504	4152	4199	614	4222	4263
481	4129	4176	493	4101	4142
458	4106	4153	456	4064	4105
434	4082	4129	427	4035	4076
401	4049	4096	404	4012	4053
380	4028	4075	379	3987	4028
302	3950	3997	357	3965	4006
			318	3926	3967

511

512 Table 4. Comparison of some combination bands for both lizardite (x = 0) and nepouite (x = 3)
513 end-members. Letters correspond to MIR features which correspond to the equivalent vibrational
514 groups for each end-member. † corresponds to small identified features (see Fig. 7).

lizardite (x = 0)		Combinations from equivalent vibrational groups	nepouite (x = 3)	
Band #	Observed NIR bands (cm^{-1})		Observed NIR bands (cm^{-1})	Band #
1	3958	a + h	3934	1
3	4001	a + i	3971	2
4	4032	b + h		
6	4077	b + i	4000	3
		d + h	4037†	4†
7	4121	d + i	4071†	6†
8	4163	e + i	4097	7
21	4781	g + i	4722	21

515

Table 5. Calculated NIR combination band positions (4300 - 4800 cm^{-1}) for lizardite (x = 0) from combination with one MIR feature and one NIR feature. Δ corresponds to the difference between the calculated and the observed combination band positions. *in letter in MIR spectra (Fig. 8) and in integer in NIR spectrum (Fig. 7). † corresponds to small identified features (see Fig. 7a).

Band #	Observed NIR bands (cm^{-1})	Combination with one MIR band and one NIR band (cm^{-1})				Calculated NIR bands (cm^{-1})	Δ (cm^{-1})	Observed features involved*
13	4363	380	+	3985	=	4365	2	b ; 2
		401	+	3958	=	4359	4	c ; 1
15	4409	380	+	4032	=	4412	3	b ; 4
		401	+	4001	=	4402	7	c ; 3
		434	+	3985	=	4419	10	d ; 2
		458	+	3958	=	4416	7	e ; 1
16	4442	401	+	4032	=	4433	9	c ; 4
		401	+	4049	=	4450	8	c ; 5
		434	+	4001	=	4435	7	d ; 3
		458	+	3985	=	4443	1	e ; 2
		481	+	3958	=	4439	3	-
17†	4487†	401	+	4077	=	4478	9	c ; 6
		434	+	4049	=	4483	4	d ; 5
		458	+	4032	=	4490	3	e ; 4
		481	+	4001	=	4482	5	-
		504	+	3985	=	4489	2	-
18†	4531†	401	+	4121	=	4522	9	c ; 7
		458	+	4077	=	4535	4	e ; 6
		481	+	4049	=	4530	1	-
		504	+	4032	=	4536	5	-
		554	+	3985	=	4539	8	-

Table 6. Calculated NIR combination band positions (4300 - 4800 cm^{-1}) for nepouite (x = 3) from combination with one MIR feature and one NIR feature. Δ corresponds to the difference between the calculated and the observed combination band positions. *in letter in MIR spectra (Fig. 8) and in integer in NIR spectrum (Fig. 7). † corresponds to small identified features (see Fig. 7b).

Band #	Observed NIR bands (cm^{-1})	Combination with one MIR band and one NIR band (cm^{-1})				Calculated NIR bands (cm^{-1})	Δ (cm^{-1})	Observed features involved*
14	4348	318	+	4037	=	4355	7	a ; 4
		357	+	4000	=	4357	9	b ; 3
		379	+	3971	=	4350	2	c ; 2
		404	+	3934	=	4338	10	d ; 1
15	4383	318	+	4056	=	4374	9	a ; 5
		318	+	4071	=	4389	6	a ; 6
		379	+	4000	=	4379	4	c ; 3
		404	+	3971	=	4375	8	-
		456	+	3934	=	4390	7	e ; 1
16†	4426†	357	+	4071	=	4428	2	b ; 6
		379	+	4037	=	4416	10	c ; 4
		379	+	4056	=	4435	9	c ; 5
		427	+	4000	=	4427	1	d ; 3
		456	+	3971	=	4427	1	e ; 2
		493	+	3934	=	4427	1	-
17	4447	318	+	4136	=	4454	7	a ; 8
		357	+	4097	=	4454	7	b ; 7
		379	+	4071	=	4450	3	c ; 6
		404	+	4037	=	4441	6	-
		456	+	4000	=	4456	9	e ; 3
18†	4522†	379	+	4136	=	4515	7	c ; 8
		379	+	4150	=	4529	7	c ; 9
		427	+	4097	=	4524	2	d ; 7
		456	+	4056	=	4512	10	e ; 5
		456	+	4071	=	4527	5	e ; 6
		493	+	4037	=	4530	8	-

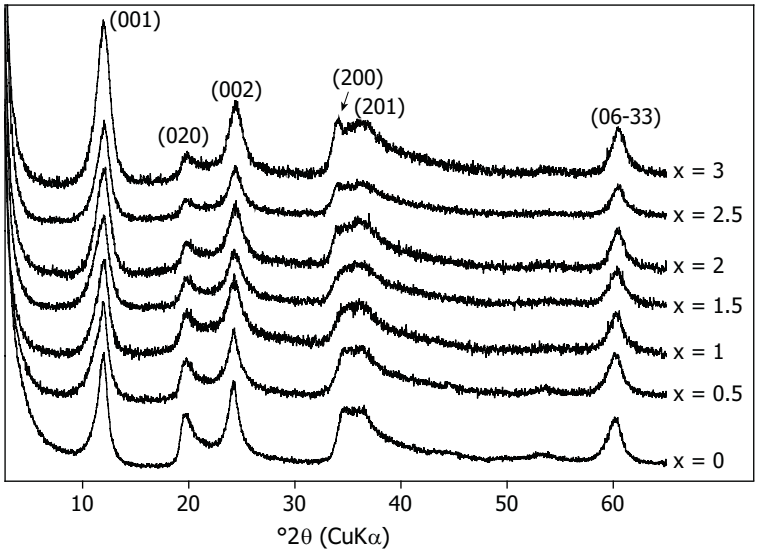
(001)
(020)
(002)
(200)
(201)
(06-33)
x = 3
x = 2.5
x = 2
x = 1.5
x = 1
x = 0.5
x = 0
10
20
30
40
50
60
°2θ (CuKα)

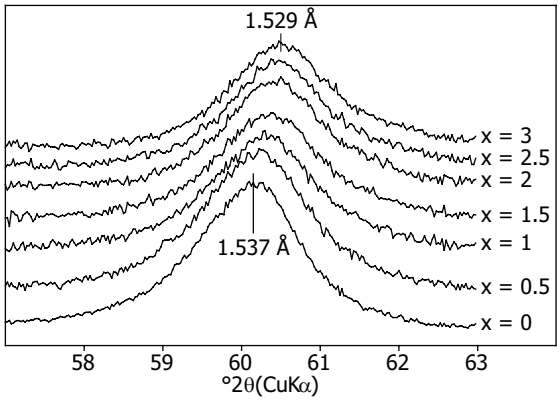
1.529 Å
1.537 Å
x = 3
x = 2.5
x = 2
x = 1.5
x = 1
x = 0.5
x = 0
58
59
60
61
62
63
°2θ(CuKα)

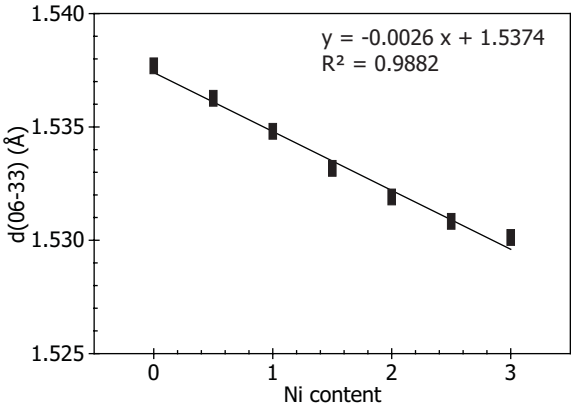
y = -0.0026 x + 1.5374
R² = 0.9882
d(06-33) (Å)
1.540
1.535
1.530
1.525
0
1
2
3
Ni content

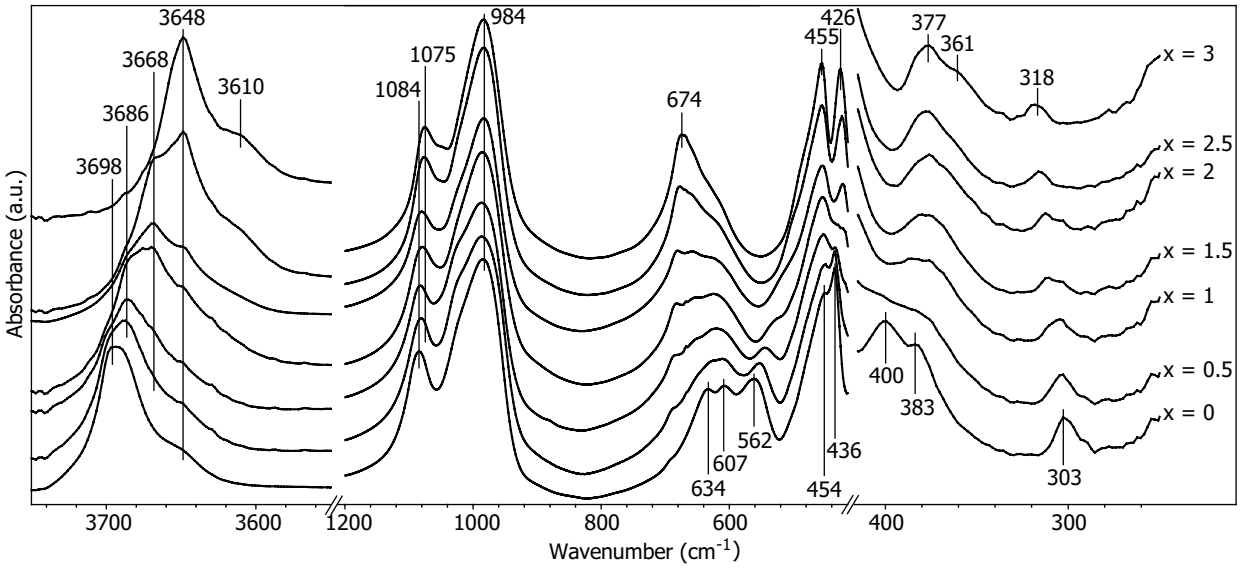
3648
3668
3610
3686
3698
984
1075
1084
674
426
455
377
361
318
x = 3
x = 2.5
x = 2
x = 1.5
x = 1
x = 0.5
x = 0
400
383
562
607
634
436
454
303
Absorbance (a.u.)
3700
3600
1200
1000
800
600
400
300
Wavenumber (cm-1)

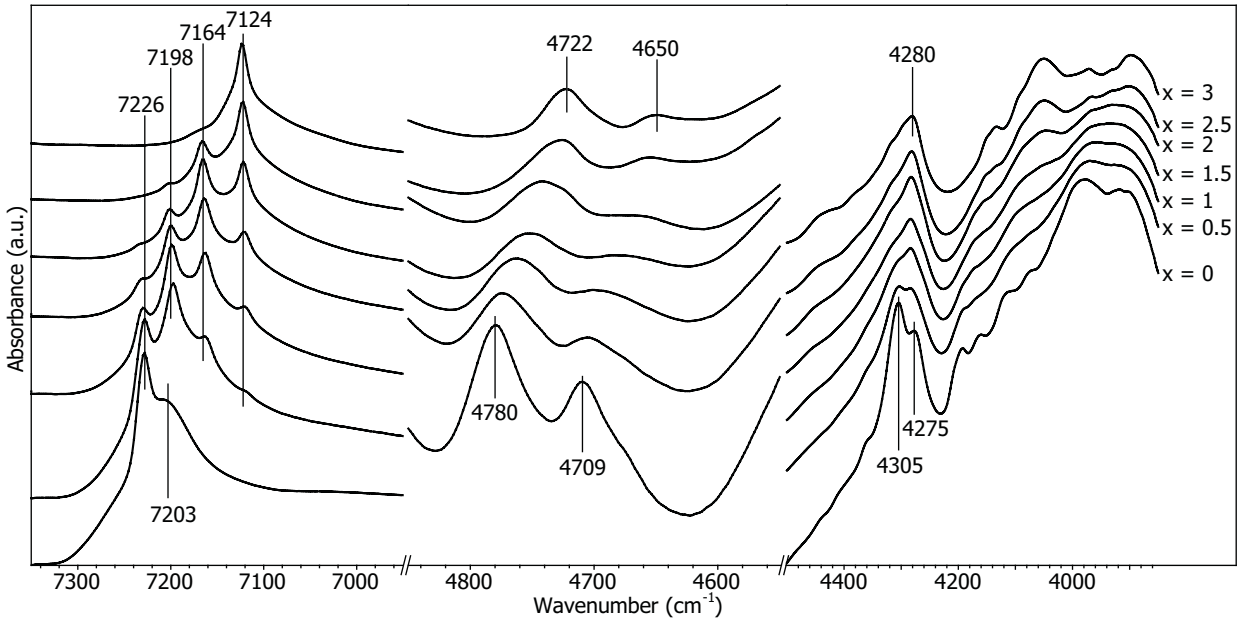
7124
7164
7198
7226
7203
4722
4650
4780
4709
4280
4275
4305
x = 3
x = 2.5
x = 2
x = 1.5
x = 1
x = 0.5
x = 0
Absorbance (a.u.)
7300
7200
7100
7000
4800
4700
4600
4400
4200
4000
Wavenumber (cm-1)

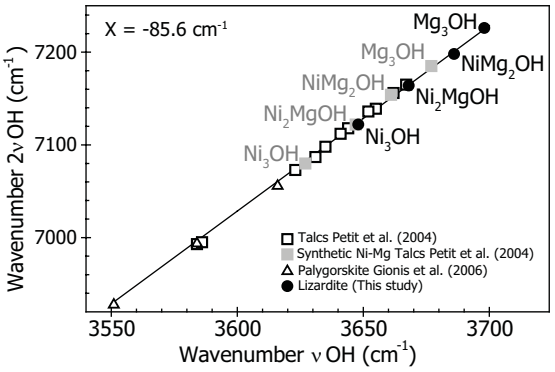
X = -85.6 cm-1
Mg3OH
Mg3OH
NiMg2OH
NiMg2OH
Ni2MgOH
Ni2MgOH
Ni3OH
Ni3OH
Talcs Petit et al. (2004)
Synthetic Ni-Mg Talcs Petit et al. (2004)
Palygorskite Gionis et al. (2006)
Lizardite (This study)
7200
7100
7000
3550
3600
3650
3700
Wavenumber 2ν OH (cm-1)
Wavenumber ν OH (cm-1)

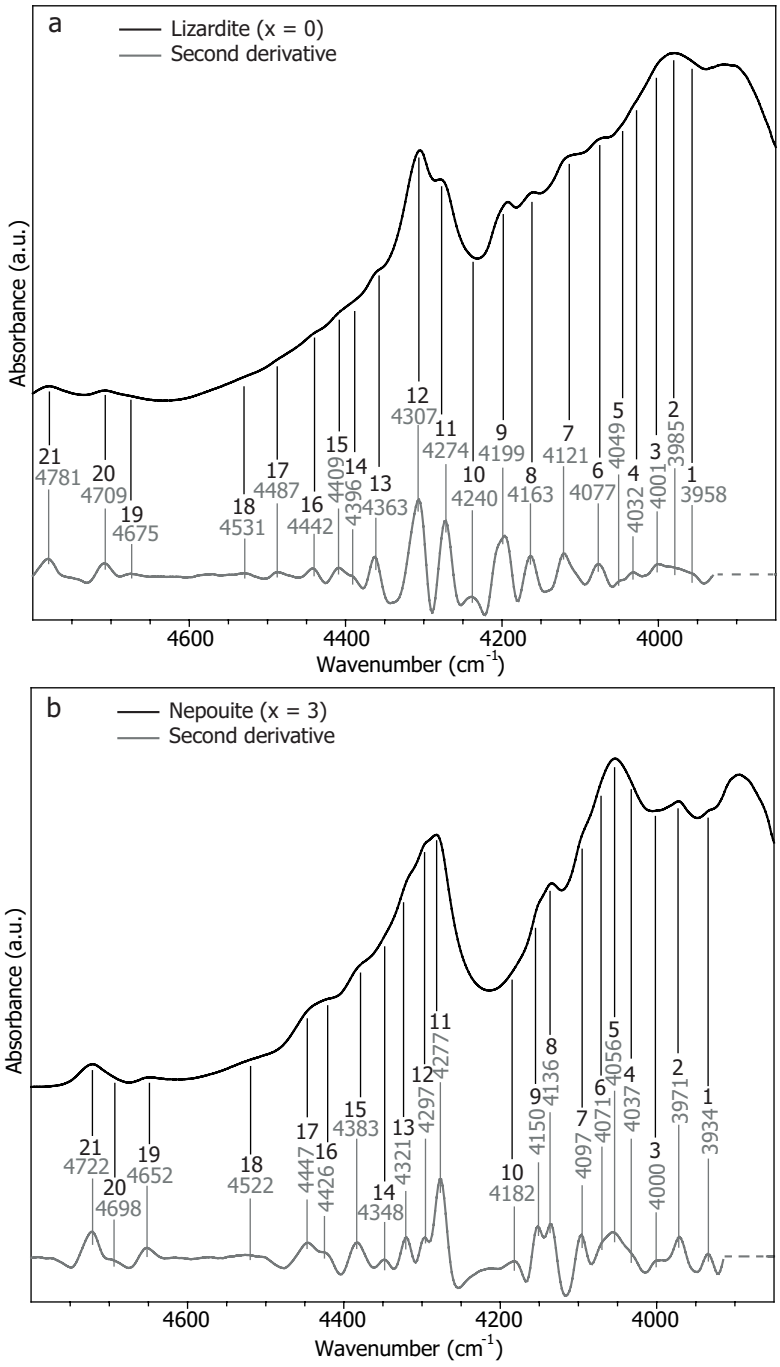
a
Lizardite (x = 0)
Second derivative
Absorbance (a.u.)
21 4781
20 4709
19 4675
18 4531
17 4487
16 4442
15 4409
14 4396
13 4363
12 4307
11 4274
10 4240
9 4199
8 4163
7 4121
6 4077
5 4049
4 4032
3 4001
2 3985
1 3958
4600
4400
4200
4000
Wavenumber (cm-1)
b
Nepouite (x = 3)
Second derivative
Absorbance (a.u.)
21 4722
20 4698
19 4652
18 4522
17 4447
16 4426
15 4383
14 4348
13 4321
12 4297
11 4277
10 4182
9 4150
8 4136
7 4097
6 4071
5 4056
4 4037
3 4000
2 3971
1 3934
4600
4400
4200
4000
Wavenumber (cm-1)

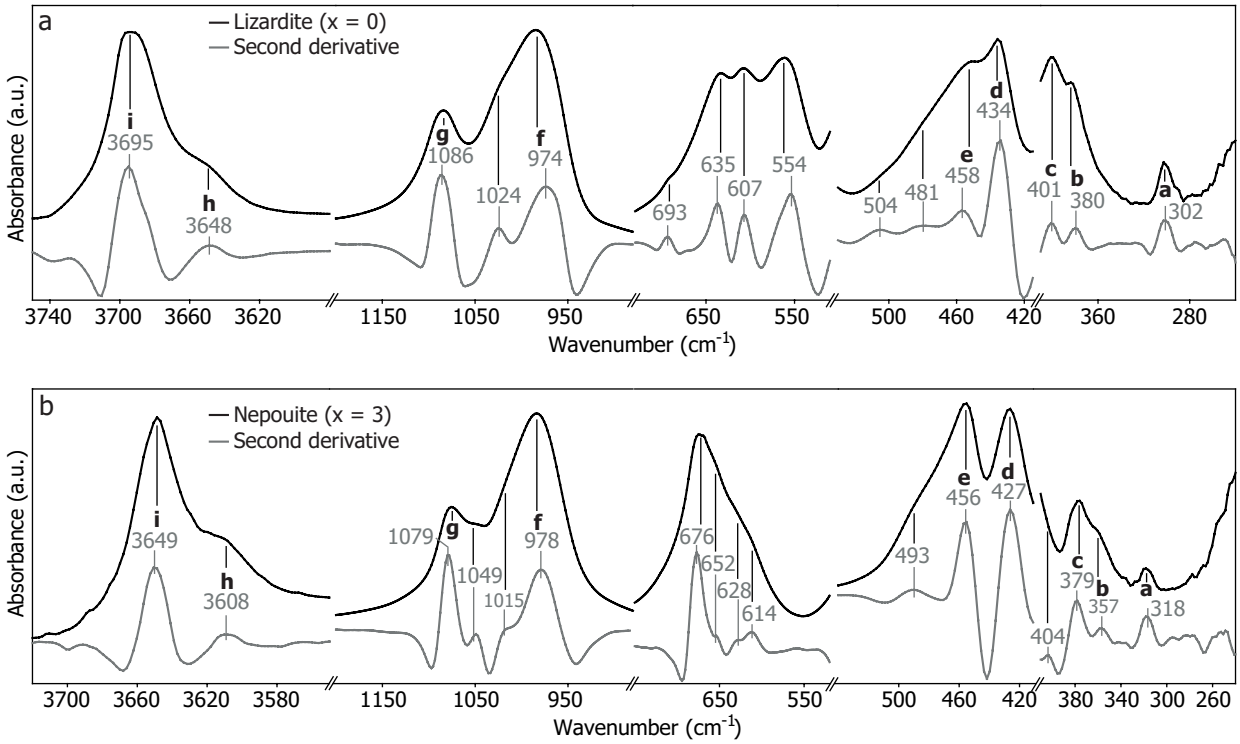
a
Lizardite (x = 0)
Second derivative
Absorbance (a.u.)
i
3695
h
3648
g
1086
f
974
1024
693
635
607
554
504
481
e
458
d
434
c
401
b
380
a
302
3740 3700 3660 3620
1150 1050 950
650 550
500 460 420 360 280
Wavenumber (cm-1)
b
Nepouite (x = 3)
Second derivative
Absorbance (a.u.)
i
3649
h
3608
1079
g
1049
1015
f
978
676
652
628
614
493
e
456
d
427
404
c
379
b
357
a
318
3700 3660 3620 3580
1150 1050 950
650 550
500 460 420 380 340 300 260
Wavenumber (cm-1)

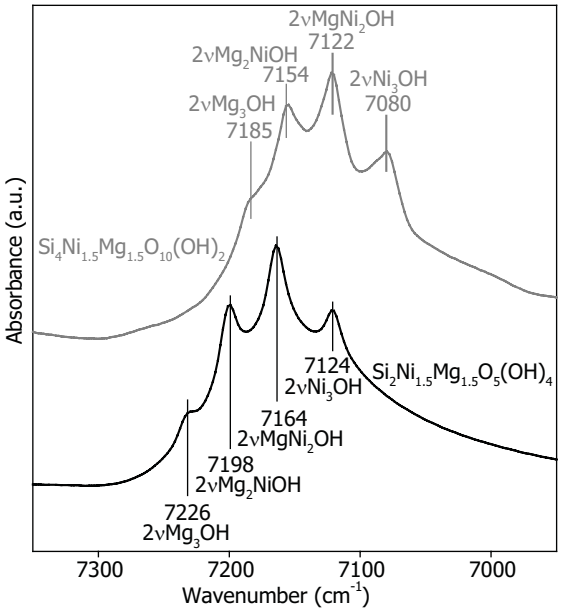
2νMgNi2OH
7122
2νMg2NiOH
7154
2νNi3OH
7080
2νMg3OH
7185
Si4Ni1.5Mg1.5O10(OH)2
Absorbance (a.u.)
7124
2νNi3OH
Si2Ni1.5Mg1.5O5(OH)4
7164
2νMgNi2OH
7198
2νMg2NiOH
7226
2νMg3OH
7300
7200
7100
7000
Wavenumber (cm-1)